Transport properties of thin flakes of the antiferromagnetic topological insulator $MnBi_2Te_4$

Jianhua Cui,[1] Mengzhu Shi,[1] Honghui Wang,[1] Fanghang Yu,[1] Tao Wu,[1,2] Xigang Luo,[1,2] Jianjun Ying,[1,*] and Xianhui Chen[1,2,†]

[1]*Hefei National Laboratory for Physical Sciences at Microscale and Department of Physics, and Chinese Academy of Sciences Key Laboratory of Strongly-Coupled Quantum Matter Physics, University of Science and Technology of China, Hefei, Anhui 230026, China*

[2]*Collaborative Innovation Center of Advanced Microstructures, Nanjing University, Nanjing 210093, China*

(Received 14 February 2019; published 12 April 2019)

$MnBi_2Te_4$ was recently suggested as the first example of an antiferromagnetic topological insulator. However, lacking good quality of single crystals hindered its further investigation. Here, we report the detailed transport properties of several $MnBi_2Te_4$ thin flakes in which samples are more homogeneous as compared to the bulk single crystals. We found all the samples exhibit antiferromagnetic transition around 25 K and the same field-driven magnetic transitions; however, temperature dependence of resistivities shows either insulating or metallic behaviors. Such behavior is in contrast with the as-grown thick single crystals in which only metallic behavior was observed. The Hall coefficients indicate the gradual decrease of the carrier density with decreasing the temperature for the sample with insulating behavior. Such difference may relate to different impurity content (antisite defects and/or Mn vacancies). Our findings indicate the bulk carrier can be localized at low temperature by introducing disorder while the magnetic ordering keeps invariant, which is quite crucial for realizing the theoretical proposed quantum anomalous Hall effect and axion insulators in this material.

DOI: 10.1103/PhysRevB.99.155125

I. INTRODUCTION

The quantum anomalous Hall (QAH) effect is a quantized Hall effect without any external magnetic field, which has attracted tremendous attention for its potential application in electronic and spintronic devices due to the dissipationless spin-polarized chiral edge states [1–11]. Magnetism and topological electronic states are two prerequisites for realizing a QAH state. QAH effect was realized in Cr- or V-doped $(Bi, Sb)_2Te_3$ magnetic topological thin films after it had been sought for over two decades [3,4,12]. However, extremely low temperature (usually <100 mK) is required by the QAH effect due to randomly distributed magnetic impurities, which would induce strong inhomogeneity in the electronic structure and magnetic properties [13]. Thus, intrinsic magnetic topological insulators with homogeneous electronic and magnetic properties are highly desired and would possibly increase the QAH working temperature. One of the candidates is the recently discovered $MnBi_2Te_4$ [14–19].

$MnBi_2Te_4$ is a stoichiometric tetradymite-type compound with the space group R-3*m* [20]. This compound is a layered material with Te-Bi-Te-Mn-Te-Bi-Te septuple layers (SLs) stacking along the *c* axis. Each SL is formed from the intercalation of a MnTe bilayer into a quintuple layer of Bi_2Te_3. SLs are coupled through van der Waals bonding, thus this material can be thinned down to two-dimensional atomic thin layers through microexfoliation. $MnBi_2Te_4$ was suggested as the first example of an antiferromagnetic topological insulator (AFM TI) recently [14–19]. An interlayer AFM ordering in $MnBi_2Te_4$ makes it invariant with respect to the *S* symmetry. *S* stands for a combined symmetry, defined as $S = \Theta T_{1/2}$, where Θ represents time-reversal symmetry and $T_{1/2}$ denotes primitive-lattice transition symmetry [15,16]. However, for the (001) cleavage surface plane, its ferromagnetic surface would break the *S* symmetry and an out-of-plane magnetization component would open a gap in the Dirac cone. A thin film of such an AFM TI with FM surfaces is expected to be an intrinsic QAH insulator or axion insulator depending on the film thickness [16,18,21]. In experiment, such a gapped Dirac cone has indeed been probed in the angle-resolved photoemission spectroscopy experiment for single-crystal samples with the gap magnitude $\sim$70 meV at the Γ point, consistent with the theoretically calculated results [14]. However, such a gap remains open even up to room temperature for single-crystal samples, in strong contrast with the molecular beam epitaxy grown $MnBi_2Te_4$ thin films which show a gapless Dirac cone at temperature above T_N [17]. Such discrepancy is possibly due to the antisite defects and Mn vacancies in the single-crystal samples [22].

Previous transport and magnetic measurements on $MnBi_2Te_4$ single crystals revealed the AFM transition with Neel temperature $T_N \sim 25$ K and the AFM state would first evolve into a canted antiferromagnetic (CAFM) state prior to the polarized FM state with the magnetic field along the out-of-plane direction [14,22,23]. Since $MnBi_2Te_4$ is metastable and would decompose to $MnTe_2$ and Bi_2Te_3 above 423 K [20], its single crystals are difficult to grow, and only small size single crystals can be isolated from the quenched ingots. These single crystals would contain antisite defects and Mn vacancies which may cause inhomogeneity in the sample [22]. Here, by microexfoliation of the $MnBi_2Te_4$ single crystals, we

*yingjj@ustc.edu.cn
†chenxh@ustc.edu.cn

 ©2019 American Physical Society

performed the magnetotransport measurements on some $MnBi_2Te_4$ thin flakes with thickness around 100–200 nm. Although all the samples exhibit antiferromagnetic transition at around 25 K and the same field-driven magnetic transitions, their temperature dependences of resistivities show either insulating or metallic behaviors. Such difference may relate to the slightly different impurity value in the sample. The Hall coefficient also indicates the reduction of carrier density at low temperature for the insulating behavior samples. These discoveries indicate the bulk carrier can be localized, which is quite crucial for realizing the QAH state in this material, and we assume that antisite defects and Mn vacancies introduce disorder in the samples which causes the localization. We observed insulating behavior in $MnBi_2Te_4$ single crystal, which was never reported in the bulk samples.

II. METHODS

The $MnBi_2Te_4$ crystals were synthesized through a solid-state reaction of Mn powder, Bi lump, and Te lump followed by a water quenching process. Mn powder, Bi lump, and Te lump were mixed with the molar ratio of 1:2:4 into the silica container in an argon gas glovebox. The above mixture was sealed and reacted in a self-built vertical Bridgman furnace. The temperature was ramped to 1100 °C in 400 min, which was kept for 48 h; then the temperature was cooled to 900 °C in 48 h and further cooled to 700 °C in 72 h, which was kept for another 72 h. Finally, the ampoule was quenched in water quickly. $MnBi_2Te_4$ single crystals could be cleaved from the product. Only (00L) peaks can be detected in the x-ray-diffraction (XRD) pattern for an as-grown single crystal as shown in Fig. 1(a). To avoid the contamination of the flux and inhomogeneity in the as-grown single crystals, we used exfoliated thin flakes for all the magnetotransport measurements. The compositions of crystals were determined using an energy-dispersive x-ray spectrometer (EDS) mounted on the field emission scanning electronic microscope, Sirion200.

To obtain $MnBi_2Te_4$ thin flakes, we mechanically exfoliated the $MnBi_2Te_4$ bulk single crystals using scotch tape, then pasted the tape onto a Si wafer which was covered with a 285-nm-thick thermally grown SiO_2 layer. Once we tore off the tape rapidly, some flakes became captured on the wafer's surface. Then we selected thin flakes using an optical microscope. The thickness was first determined by atomic force microscopy. After thin flakes (thickness between 100 and 200 nm) were identified on the substrate, we used lithography to prepare resist masks of a standard Hall bar configuration on top of the flakes as the contact regions. This was followed by deposition of 150-nm Au (with a 10-nm Cr underlayer) and the standard liftoff procedures. All the magnetotransport measurements were performed using the Quantum Design PPMS-9. Atomic force microscopy data were taken with Park Systems NX10.

III. RESULTS AND DISCUSSION

In Fig. 1(a), the XRD pattern of an as-grown single crystal shows the sharp (00L) x-ray-diffraction peaks matched well with the ICDD database PDF card 04-020-8214 [20], revealing phase-pure $MnBi_2Te_4$ with a strongly preferred

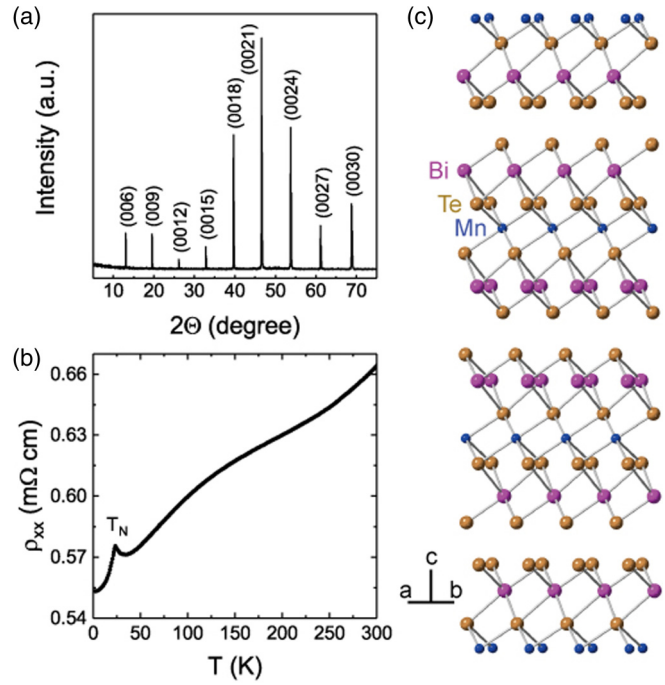

FIG. 1. Structural characterizations and transport properties of as-grown $MnBi_2Te_4$ single crystals. (a) XRD pattern of as-grown $MnBi_2Te_4$ single crystals. Note strong preferred orientation along [001]. (b) In-plane electrical resistivity of a single crystal measured from room temperature down to 2 K. All the as-grown crystals show metallic behaviors and antiferromagnetic transitions with $T_N = 25$ K. (c) Atomic structure of the R-3m-group bulk $MnBi_2Te_4$ with purple, brown, and blue balls showing Bi, Te, and Mn atoms, respectively.

orientation along the [001] direction. The crystal structure of $MnBi_2Te_4$ is shown in Fig. 1(c). We cannot detect any impurity peaks in the XRD pattern indicating the as-grown single crystal is pure. All the as-grown crystals show metalliclike behaviors with the temperature decreasing from 300 to 2 K as shown in Fig. 1(b). A well-defined kink at 25 K indicates a magnetic transition which is consistent with the previous transport measurements [14,22,23].

As mentioned before, antisite defects and Mn vacancies contained in as-grown bulk crystals may cause inhomogeneity in the sample, so we carried out measurements on thin flakes which are more homogeneous due to their small size. Figure 2(a) shows an optical image of a typical $MnBi_2Te_4$ thin-flake device. $MnBi_2Te_4$ thin flakes were obtained by mechanically exfoliating the bulk single crystals using the scotch tape and transferring them onto the substrate. The surface of the thin flake was checked by the atomic force microscopy as shown in Fig. 2(b), and the thickness of the sample is about 180 nm as shown in Fig. 2(c). The thicknesses of all the samples measured in this experiment are around 100–200 nm. Figures 2(d) and 2(e) show the element map for Bi and Mn, respectively, using EDS on a scanning electron microscope. Our results indicate that these two elements distribute homogeneously in our samples.

Figure 3 presents the temperature dependences of the in-plane resistivity (ρ_{xx}) of two different samples. Two samples

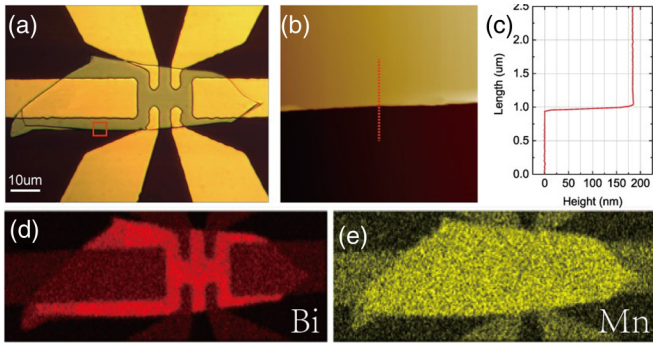

FIG. 2. (a) The optical image of a typical exfoliated $MnBi_2Te_4$ thin flake with a standard Hall bar configuration. The device is made by lithography and liftoff techniques. The scale bar equals to 10 μm. (b) Atomic force microscopy image of the square marked in (a). The sample surface is quite smooth. (c) Line profile along the dashed line shown in (b), indicating the sample thickness is around 180 nm. (d, e) Elemental maps of Bi (red) and Mn (yellow) by scanning EDX. The scanning maps indicate homogeneous distribution of Bi and Mn in the sample.

exhibit the same antiferromagnetic transition at around 25 K, while showing either metallic or insulating behaviors. The resistivity peaks near T_N can be well understood in terms of spin scattering due to spin fluctuations. For a local-moment AFM like $MnBi_2Te_4$, the intensified spin fluctuations due to spin-wave excitations near T_N can greatly affect transport properties [24]. The discovery of two different resistivity behaviors in the thin flake samples is the key finding in this paper. Since the thin flake samples are more homogeneous than the as-grown single crystals, such insulating behavior was never observed in the bulk single-crystal samples in which the resistivity is possibly dominated by the metallic channel.

To further verify the mechanism of the difference between these two samples, we systematically measured the variation

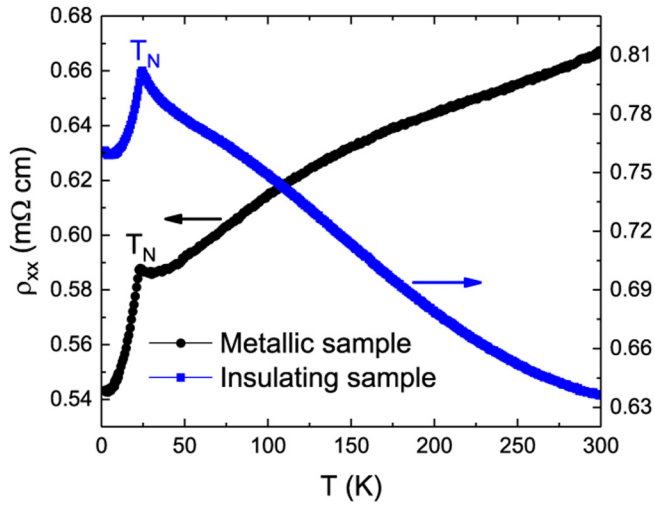

FIG. 3. Temperature dependences of the in-plane resistivity $\rho_{xx}(T)$ for two different thin flake samples. One shows metallic behavior, while the other one shows insulating behavior. Both samples show an antiferromagnetic transition with $T_N = 25$ K.

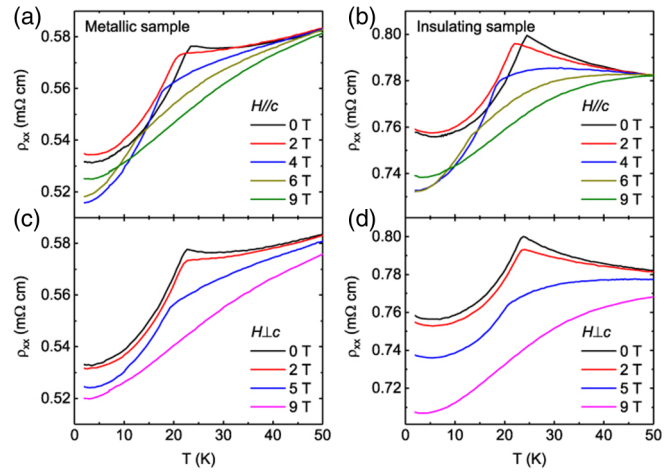

FIG. 4. Temperature dependences of the in-plane resistivity $\rho_{xx}(T)$ under various magnetic fields for two different thin flake samples. (a, b) $\rho_{xx}(T)$ under various magnetic fields along the c axis for the metallic sample (a) and insulating sample (b). (c, d) $\rho_{xx}(T)$ under various magnetic fields perpendicular to the c axis for the metallic sample (c) and insulating sample (d). Peaks near T_N in $\rho_{xx}(T)$ for both samples are suppressed by increasing the magnetic fields. The $\rho_{xx}(T)$ of two samples show similar behaviors.

of resistivity under external magnetic field applied along out-of-plane and in-plane directions, respectively. Figures 4(a)–4(d) show that the peaks near T_N in both insulating and metallic samples shift to lower temperatures as the field increases and can be suppressed completely at high field. This observation is consistent with the spin-fluctuation-driven spin scattering scenario [23]. In the A-type AFM system, spin scattering generated by interlayer AFM coupling results in a high-resistivity state, while strong external field can suppress it by pushing the system to a forced FM state [25,26].

We performed magnetotransport measurements of $\rho_{xx}(H)$ at various temperatures for both $H//c$ and $H\perp c$ of metallic sample and insulating sample as shown in Figs. 5(a)–5(d). For $H//c$ shown in Figs. 5(a) and 5(b), $\rho_{xx}(H)$ show notable decrease at around 3 T, which is due to the AFM-to-CAFM transition consisting with the previous measurements [23]. This CAFM state is a metastable state before the system is completely polarized to a FM state. The critical magnetic field of CAFM-to-FM transition which was indicated by the arrows decreases with increasing temperature. The critical magnetic fields as a function of temperature for both the metallic and insulating samples are shown in Fig. 6. There is no obvious disparity between two samples. For $H\perp c$ shown in Figs. 5(c) and 5(d), the steep decrease does not appear, indicating that the AFM state is gradually polarized to the FM state without undergoing a metastable CAFM state. The critical magnetic field of AFM-to-FM transition at low temperature is higher than 9 T, thus we cannot detect it in our experiment below 10 K. Furthermore, the critical field reduces with increasing temperature as well. Different behaviors of $\rho_{xx}(H)$ for $H//c$ and $H\perp c$ illustrate that its AFM state is characterized by an A-type AFM order formed by the Mn FM layers stacked antiferromagnetically along the c axis and the ordered magnetic moments are aligned in the c-axis direction. We

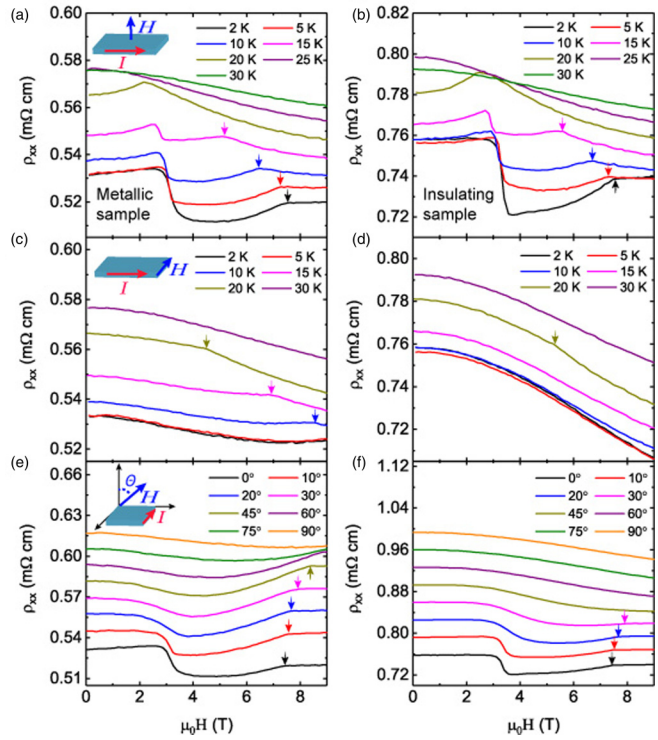

FIG. 5. Magnetotransport properties of $MnBi_2Te_4$ for the two samples. (a–d) Field dependence of in-plane resistivity $\rho_{xx}(H)$ with applied magnetic field parallel to the c axis [metallic sample (a) and insulating sample (b)] and perpendicular to the c axis [metallic sample (c) and insulating sample (d)] at various temperatures, respectively. (a, b) For $H//c$, $\rho_{xx}(H)$ show steep decrease in response to the AFM-to-CAFM transition at about 3 T. The kinks at higher magnetic field indicate the CAFM-to-FM transition. (c, d) $\rho_{xx}(H)$ show gradual decrease with increasing field for $H\perp c$ indicating the spin gradually transits from the AFM to FM. (e, f) Angular dependence of the resistivity $\rho_{xx}(H)$ (shifted vertically for clarity) at 2 K with H rotated from the out-of-plane to in-plane direction for the metallic sample (e) and insulating sample (f). The tilt angle θ is defined as the angle between H and the c-axis direction. The schematics in (a), (c), and (e) illustrate the setup of the magnetotransport experiments. The arrows indicate the kinks in $\rho_{xx}(H)$ due to the CAFM-to-FM or AFM-to-FM transitions.

also performed angular dependence of the resistivity $\rho_{xx}(H)$ measurements at 2 K with H rotated from out-of-plane to in-plane direction for two samples as shown in Figs. 5(e) and 5(f), respectively. We can see that the steep decrease of $\rho_{xx}(H)$ around 3 T was gradually reduced with H rotated from $H//c$ to $H\perp c$, and completely disappears with the tilt angle θ larger than 45 deg. The critical field of CAFM-to-FM transition shifts to higher magnetic field with H rotated from $H//c$ to $H\perp c$. These magnetotransport measurements also indicate the magnetic properties of both samples exhibit the same magnetic properties although their $\rho_{xx}(T)$ behaviors are completely different. The tiny differences of the $\rho_{xx}(H)$ behavior are possibly due to the small different antisite defects and/or Mn vacancies in these samples.

To make out the different transport properties of the samples, we also carry out Hall resistivity ρ_{xy} measurements.

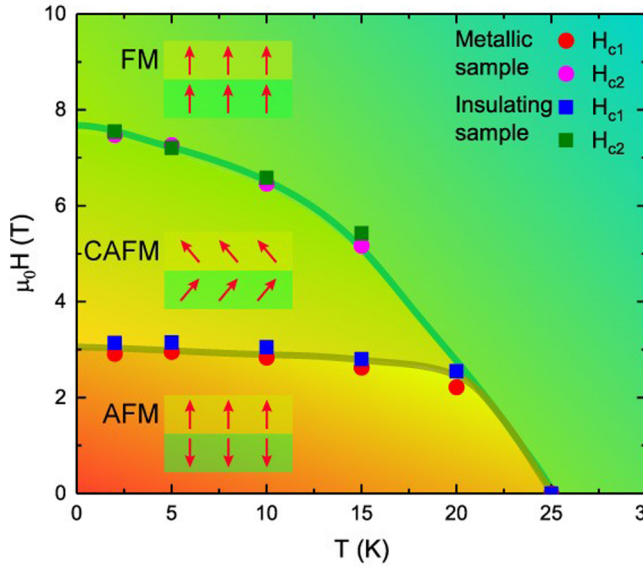

FIG. 6. The phase diagram of magnetic states in $MnBi_2Te_4$ flakes. The circles and squares represent the critical magnetic field as a function of temperature for the metallic and insulating samples, respectively. There is no obvious disparity between two kinds of samples. The corresponding arrows represent the magnetic order formed by the Mn FM layers, showing AFM, canted AFM, and FM orders, respectively.

Figures 7(a) and 7(b) show ρ_{xy} as a function of magnetic field at various temperatures. From these data, we can observe anomalous Hall effect in both samples, which is due to the AFM-CAFM transition at around 3 T. At low field, the field dependence of ρ_{xy} is quite linear because of the single-band

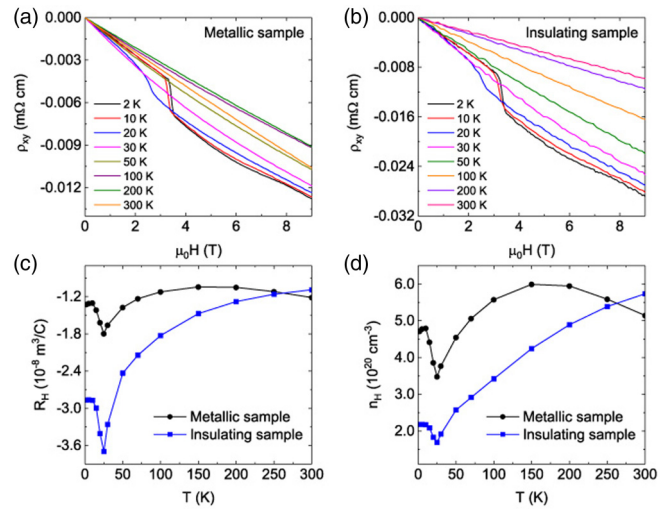

FIG. 7. Hall effect of $MnBi_2Te_4$. (a, b) Hall resistivity $\rho_{xy}(H)$ as a function of magnetic field at various temperatures for the metallic sample (a) and insulating sample (b). There is a sharp decrease of $\rho_{xy}(H)$ at around 3T in response to the AFM-to-CAFM transition for both samples. (c, d) Temperature dependence of Hall coefficient R_H and carrier density n_H. For the insulating sample, n_H obviously decreases with decreasing the temperature. For both samples, n_H shows anomaly and reaches the minimum value around T_N.

nature of this system. So we can work out the Hall coefficient R_H and carrier density n_H as shown in Figs. 7(c) and 7(d). The negative sign of R_H indicates that the carriers in our samples are electron type. The temperature dependence of carrier density of different samples shows quite different behaviors clarifying the distinctive transport properties. The n_H for the metallic sample shows weak temperature dependence similar to the normal metal. However, for a sample with insulating behavior above T_N, carrier density reduces monotonically with decreasing temperature, which indicates the localization of carrier density at low temperature. Nevertheless, in both samples the temperature dependence of carrier density shows a well-defined kink at T_N indicating invariant magnetic ordering. The Hall mobility is estimated to be about 31 and 46 $cm^2/V\,s$ for the metallic and insulating samples at 25 K, respectively.

We have found the resistivity of $MnBi_2Te_4$ thin flakes could have either insulating or metallic behaviors and measured many $MnBi_2Te_4$ thin flakes to make sure that both metallic and insulating behaviors are intrinsic in our samples. Elemental analysis has been performed to verify the chemical constituents of $MnBi_2Te_4$ samples using spot EDS analysis. Although there are two kinds of transport properties of our samples, the EDS spectrum indicates that the samples have the same stoichiometry as $Mn_{0.84}Bi_{2.10}Te_4$, which is consistent with the preceding work [22]. Although two samples show different resistivity behaviors, the magnitude of resistivity and carrier density are similar at room temperature. Thus, the Fermi energy of two samples should not change too much. The magnetoresistivity behaviors of two samples are similar and consistent with previous results performed in the thick sample [23], indicating the same magnetism in the two samples. Since the samples have similar geometries and the bulk sample shows pure phase from XRD, different behaviors of the samples cannot originate from the impurity phases and thickness effect. Previously reported structure refinement of x-ray diffraction suggests that there exists some degree of antisite defects and Mn vacancies in the single crystals [22]. These impurities or defects may vary from sample to sample and cause inhomogeneity in large sized thick samples. One possibility of the insulating behavior in resistivity for our sample is that more disorder in this sample may significantly increase the scattering rate and localize itinerant carriers at low temperature due to Anderson localization. The itinerant carriers are detrimental for realizing the QAH effect, which would destroy the QAH state by providing additional conduction channels. Actually, introducing disorder to localize itinerant carriers in a metallic system can also realize the QAH effect [27]. V-doped $(Bi, Sb)_2Te_3$, which was originally considered as a metallic FM state by first-principles calculation [5], turned out to be insulating FM and evolved into a QAH state at low temperature possibly due to the localization of the bulk carrier band by disorder [2,3]. Such carrier localization effect in $MnBi_2Te_4$ may become more significant if we can thin down the sample to few layers, thus the theoretical proposed QAH effect may be realized in few-layer $MnBi_2Te_4$ by introducing the disorder.

IV. CONCLUSION

In conclusion, we performed magnetotransport measurements on some $MnBi_2Te_4$ thin flakes. We found the normal state resistivity behavior could be either insulating or metallic with the magnetism almost identical. The carrier density of the insulating sample rapidly decreases with decreasing the temperature. We ascribed such differences to the small different antisite defects and/or Mn vacancies in the sample. Our findings indicate the bulk carrier density might be greatly reduced by varying the impurity value, which is quite crucial for realizing the theoretical proposed QAH effect and axion insulators in $MnBi_2Te_4$ thin films.

ACKNOWLEDGMENTS

This work is supported by the National Key Research and Development Program of China (Grants No. 2016YFA0300201 and No. 2017YFA0303001), the National Natural Science Foundation of China (Grants No. 11534010 and No. 11888101), the Key Research Program of Frontier Sciences of the Chinese Academy of Sciences (CAS, Grant No. QYZDY-SSW-SLH021), the Strategic Priority Research Program (B) of the CAS (Grant No. XDB25010100), Science Challenge Project (Grant No. TZ2016004), and Hefei Science Center of the CAS (Grant No. 2016HSC-IU001).

[1] C.-X. Liu, S.-C. Zhang, and X.-L. Qi, Annu. Rev. Condens. Matter Phys. **7**, 301 (2016).
[2] C. Cui-Zu and L. Mingda, J. Phys. Condens. Matter **28**, 123002 (2016).
[3] C.-Z. Chang, W.-W. Zhao, D.-Y. Kim, H.-J. Zhang, B.-A. Assaf, D. Heiman, S.-C. Zhang, C.-X. Liu, M. H. W. Chan, and J. S. Moodera, Nat. Mater. **14**, 473 (2015).
[4] C.-Z. Chang, J. Zhang, X. Feng, J. Shen, Z. Zhang, M. Guo, K. Li, Y. Ou, P. Wei, L.-L. Wang *et al.*, Science **340**, 167 (2013).
[5] R. Yu, W. Zhang, H.-J. Zhang, S.-C. Zhang, X. Dai, and Z. Fang, Science **329**, 61 (2010).
[6] C.-X. Liu, X.-L. Qi, X. Dai, Z. Fang, and S.-C. Zhang, Phys. Rev. Lett. **101**, 146802 (2008).
[7] H. Weng, R. Yu, X. Hu, X. Dai, and Z. Fang, Adv. Phys. **64**, 227 (2015).
[8] X. Kou, Y. Fan, M. Lang, P. Upadhyaya, and K. L. Wang, Solid State Commun. **215**, 34 (2015).
[9] Q.-Z. Wang, X. Liu, H.-J. Zhang, N. Samarth, S.-C. Zhang, and C.-X. Liu, Phys. Rev. Lett. **113**, 147201 (2014).
[10] K. He, Y. Wang, and Q.-K. Xue, Annu. Rev. Condens. Matter Phys. **9**, 329 (2018).
[11] G. Xu, H. Weng, Z. Wang, X. Dai, and Z. Fang, Phys. Rev. Lett. **107**, 186806 (2011).
[12] F. D. M. Haldane, Phys. Rev. Lett. **61**, 2015 (1988).
[13] X. Feng, Y. Feng, J. Wang, Y. Ou, Z. Hao, C. Liu, Z. Zhang, L. Zhang, C. Lin, J. Liao *et al.*, Adv. Mater. **28**, 6386 (2016).
[14] M. M. Otrokov *et al.*, arXiv:1809.07389.
[15] D. Zhang, M. Shi, T. Zhu, D. Xing, H. Zhang, and J. Wang, arXiv:1808.08014.

[16] J. Li, Y. Li, S. Du, Z. Wang, B.-L. Gu, S.-C. Zhang, K. He, W. Duan, and Y. Xu, arXiv:1808.08608.
[17] Y. Gong *et al.*, arXiv:1809.07926.
[18] M. M. Otrokov, I. P. Rusinov, M. Blanco-Rey, M. Hoffmann, A. Yu. Vyazovskaya, S. V. Eremeev, A. Ernst, P. M. Echenique, A. Arnau, and E. V. Chulkov, Phys. Rev. Lett. **122**, 107202 (2019).
[19] Y. Peng and Y. Xu, arXiv:1809.09112.
[20] D. S. Lee, T.-H. Kim, C.-H. Park, C.-Y. Chung, Y. S. Lim, W.-S. Seo, and H.-H. Park, Cryst. Eng. Comm. **15**, 5532 (2013).
[21] R. S. K. Mong, A. M. Essin, and J. E. Moore, Phys. Rev. B **81**, 245209 (2010).
[22] A. Zeugner *et al.*, arXiv:1812.03106.
[23] S. Huat Lee *et al.*, arXiv:1812.00339.
[24] T. J. Liu *et al.*, Phys. Rev. B **80**, 174509 (2009).
[25] M. N. Baibich, J. M. Broto, A. Fert, F. Nguyen Van Dau, F. Petroff, P. Etienne, G. Creuzet, A. Friederich, and J. Chazelas, Phys. Rev. Lett. **61**, 2472 (1988).
[26] G. Binasch, P. Grünberg, F. Saurenbach, and W. Zinn, Phys. Rev. B **39**, 4828 (1989).
[27] K. Nomura and N. Nagaosa, Phys. Rev. Lett. **106**, 166802 (2011).